Nanoscale electromagnetism with the boundary element method

Ulrich Hohenester [1,*] and Gerhard Unger [2]

[1]*Institute of Physics, University of Graz, Universitätsplatz 5, 8010 Graz, Austria*
[2]*Institute of Applied Mathematics, Technical University of Graz, Steyrergasse 30, 8010 Graz, Austria*

In Yang *et al.* [Nature **576**, 248 (2019)], the authors introduced a general theoretical framework for nanoscale electromagnetism based on Feibelman parameters. Here quantum effects of the optically excited electrons at the interface between two materials are lumped into two complex-valued and frequency-dependent parameters which can be incorporated into modified boundary conditions for Maxwell's equations, the so-called mesoscopic boundary conditions. These modifications can, in principle, be implemented in any Maxwell solver, although the technicalities can be subtle and depend on the chosen computational approach. In this paper, we show how to implement mesoscopic boundary conditions in a boundary element method approach based on a Galerkin scheme with Raviart-Thomas shape elements for the representation of the tangential electromagnetic fields at the boundary. We demonstrate that the results of our simulations are in perfect agreement with Mie theory, including Feibelman parameters, and that for typical simulation scenarios the computational overhead is usually small.

I. INTRODUCTION

Plasmonics has given photonics the ability to go to the nanoscale [1–4]. This is achieved by optically exciting coherent electron charge oscillations at the boundary of metallic nanoparticles, so-called localized surface plasmon resonances or particle plasmons in short, which come along with strongly localized evanescent fields that allow focusing electromagnetic fields to deep subwavelength volumes [5,6]. Applications are manifold and range from sensorics and photovoltaics, over catalysis and thermal management, to metamaterials. By a similar token, hybrid photon-phonon excitations at the surface of ionic nanoparticles, so-called surface phonon polaritons, enable extreme light confinement in the infrared regime [7], which is of importance for the emerging fields of phononics [8] and thermoelectrics [9], as well as for the controlled heat transfer at the nanoscale [10,11].

The theoretical description of optical excitations of metallic, ionic, or dielectric nanoparticles is based on the solution of Maxwell's equations, where the optical response of the nanoparticles is usually modeled in terms of homogeneous, local, and isotropic permittivity and permeability functions. The validity of such a classical description has been questioned from the early days of plasmonics [12], and it has become customary to coin the term quantum plasmonics for deviations from a purely classical description [13–15]. These include a nonlocal dielectric response [16–19] or quantum tunneling through subnanometer gaps between coupled nanoparticles [20,21], which can lead to charge transfer plasmons [22].

Feibelman parameters provide a general and versatile scheme to account for modifications from a classical description at nanostructure interfaces [23]. They were introduced

by Feibelman in the description of reflection and transmission of plane waves at flat interfaces. The basic idea is to model the wave propagation on both sides of the interface through solutions of Maxwell's equations using homogeneous and local permittivities and to lump all quantum effects of the metal electrons in the vicinity of the surface, say, in a region of about one nanometer, into two so-called Feibelman parameters. These parameters $d_\perp(\omega)$, $d_\parallel(\omega)$ are usually complex valued and frequency dependent and can be interpreted in terms of charge and current distribution displacements of optically excited metal electrons [6,23,24]. Feibelman parameters were brought to the field of plasmonics in Ref. [25], where the authors showed that they can accommodate d-band effects in transition metals and explain the somewhat counterintuitive blue shift of surface plasmon resonances.

Recently, Yang *et al.* [26] suggested a methodology to incorporate Feibelman parameters into a framework based on Maxwell's equations with modified boundary conditions

$$D_2^\perp - D_1^\perp = d_\parallel \nabla_\parallel \cdot (\boldsymbol{D}_2^\parallel - \boldsymbol{D}_1^\parallel), \tag{1a}$$

$$B_2^\perp - B_1^\perp = 0, \tag{1b}$$

$$\boldsymbol{E}_2^\parallel - \boldsymbol{E}_1^\parallel = -d_\perp \nabla_\parallel (E_2^\perp - E_1^\perp), \tag{1c}$$

$$\boldsymbol{H}_2^\parallel - \boldsymbol{H}_1^\parallel = -i\omega d_\parallel \hat{\boldsymbol{n}} \times (\boldsymbol{D}_2^\parallel - \boldsymbol{D}_1^\parallel), \tag{1d}$$

where all modifications of the electronic response at the interface are encompassed in $d_\perp(\omega)$, $d_\parallel(\omega)$. The beauty of Eq. (1) is that the quantum effects at the interface are described on the same footing as the bulk material properties, namely, in terms of effective parameters, which are extracted from either experiment or first principles calculation. While the bulk permittivity function is usually obtained from a coarse graining procedure [27], which can incorporate quantum effects, the Feibelman parameters are obtained from quantum descriptions for the electron wave functions at the metal

surface, using either simplified Drude or more realistic many-body models [15,23]. The framework for the consideration of quantum effects within Maxwell's equations through Feibelman parameters has been denoted as nanoscale electromagnetism and the boundary conditions of Eq. (1) have been referred to as mesoscopic boundary conditions [26].

Although the solutions of Maxwell's equations with mesoscopic boundary conditions have provided good agreement with experiment and complementary theoretical descriptions [15,24,26], the implementation of the mesoscopic boundary conditions into available homemade or commerical Maxwell solvers proves to be nontrivial. In Ref. [26], the authors employed an iterative solution scheme using the standard boundary conditions of tangential electromagnetic fields [27], where the right-hand sides of Eq. (1) were accounted for through additional surface charge and current distributions, which were successively updated until convergence was reached. Alternatively, the authors suggested a scheme based on resonance or quasinormal modes [28–32], where the modifications due to the mesoscopic boundary conditions were included in a kind of perturbation approach within lowest order.

In this paper, we develop a methodology for the solution of Maxwell's equations using a boundary element method (BEM) approach together with the mesoscopic boundary conditions of Eq. (1), and implement the modifications in our homemade Maxwell solver NANOBEM. We demonstrate the applicability of our implementation for a few proof-of-principle simulations. Quite generally, the BEM appears to be particularly well-suited for the consideration of Feibelman parameters, as it precisely assumes solutions of the homogeneous Maxwell equations (with local and homogenous material properties) on both sides of an interface and matches in a second step the fields across the interface using the boundary conditions.

We have organized our paper as follows. In Sec. II, we develop the methodology for nanoscale electromagnetism within the BEM approach. We use the usual Stratton-Chu approach for the tangential electromagnetic fields [6,33,34], together with a Galerkin scheme using Raviart-Thomas shape elements. As in our implementation of mesoscopic boundary conditions, we will use some technicalities of the Galerkin scheme—we present the BEM methodology in more length than probably needed, mainly to keep our paper as self-contained as possible. In Sec. III, we present a few selected examples for nanophotonics simulations, including mesoscopic boundary conditions, and demonstrate that our results are in perfect agreement with Mie theory. Finally, in Sec. IV we discuss the computational cost of our approach and briefly summarize our paper.

II. THEORY

A. Boundary integral method

The starting point of the boundary integral method is the dyadic Green's function

$$\overset{\leftrightarrow}{G}_j(\mathbf{r}, \mathbf{r}') = \left(\overset{\leftrightarrow}{I} + \frac{\nabla\nabla}{k_j^2} \right) \frac{e^{ik_j|\mathbf{r}-\mathbf{r}'|}}{4\pi|\mathbf{r}-\mathbf{r}'|}, \qquad (2)$$
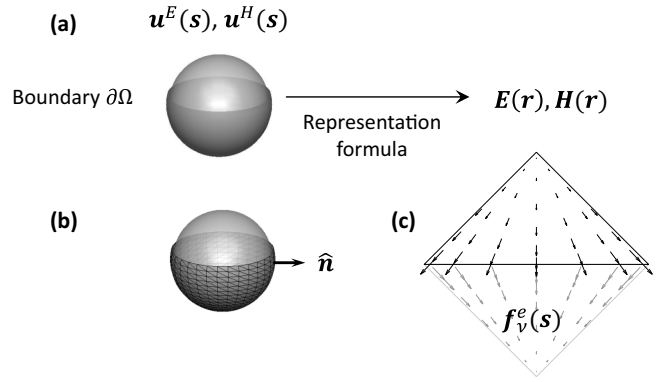

FIG. 1. Schematics of (a) boundary integral method and (b) boundary element method. (a) We consider a nanoparticle with a homogeneous and local permittivity function $\varepsilon_1(\omega)$ that is embedded in a background medium with permittivity $\varepsilon_2(\omega)$. The sharp nanoparticle boundary is denoted with $\partial\Omega$ and the outer surface normal with $\hat{\mathbf{n}}$. Once the tangential electromagnetic fields $\mathbf{u}^{E,H}$ are known at the boundary, they can be computed everywhere else using the representation formula of Eq. (4). (b) In the boundary element method, the nanoparticle boundary is discretized using boundary elements of triangular shape and (c) the tangential electromagnetic fields are approximated using Raviart-Thomas shape elements $\mathbf{f}_\nu^e$. The working equations can be expressed in the form of matrix-vector multiplications, and the solutions $\mathbf{u}^{E,H}$ are obtained through matrix inversion.

where k_j is a wave number, $\overset{\leftrightarrow}{I}$ the unit matrix, and we have used the outer product with $(\nabla\nabla)_{ij} = \partial_i\partial_j$. Within an unbounded medium, the electric field $\mathbf{E}_{\mathrm{inc}}(\mathbf{r})$ due to a current distribution $\mathbf{J}(\mathbf{r}')$ can then be expressed as [6]

$$\mathbf{E}_{\mathrm{inc}}(\mathbf{r}) = i\mu_0\omega \int \overset{\leftrightarrow}{G}_j(\mathbf{r}, \mathbf{r}') \cdot \mathbf{J}(\mathbf{r}') \, d^3r', \qquad (3)$$

where μ_0 is the permeability of free space (we consider non-magnetic materials only) and ω is the angular frequency of the oscillating current distribution. Thus, the Green's function is proportional to the electric field at position $\mathbf{r}$ generated by a unit current source at position $\mathbf{r}'$. For reasons to become clear in a moment, we denote $\mathbf{E}_{\mathrm{inc}}(\mathbf{r})$ as an incoming field.

In what follows, we consider the situation depicted in Fig. 1 of a nanoparticle with permittivity ε_1, which may depend on frequency ω, embedded in a background medium with permittivity ε_2. In principle, our formalism also applies to geometries of coupled or coated particles, as long as the permittivity functions ε are local, homogeneous, and isotropic, but we here discuss the situation of a single particle only. Following the seminal work of Stratton and Chu [33], we express the electric field $\mathbf{E}(\mathbf{r})$ outside the nanoparticle in terms of the tangential electromagnetic fields $\hat{\mathbf{n}} \times \mathbf{E}$, $\hat{\mathbf{n}} \times \mathbf{H}$ at the nanoparticle boundary $\partial\Omega$ through (see also Ref. [6, Eq. (5.26)])

$$\mathbf{E}(\mathbf{r}) = \mathbf{E}_{\mathrm{inc}}(\mathbf{r}) + \oint_{\partial\Omega} \left\{ i\mu_0\omega \overset{\leftrightarrow}{G}_2(\mathbf{r}, \mathbf{s}') \cdot \hat{\mathbf{n}}' \times \mathbf{H}(\mathbf{s}') \right.$$

$$\left. - [\nabla' \times \overset{\leftrightarrow}{G}_2(\mathbf{r}, \mathbf{s}')] \cdot \hat{\mathbf{n}}' \times \mathbf{E}(\mathbf{s}') \right\} dS'. \qquad (4)$$

Here $\mathbf{E}_{\mathrm{inc}}(\mathbf{r})$ is the incoming field of Eq. (3) produced by the current distribution in the embedding medium, $\hat{\mathbf{n}}$, $\hat{\mathbf{n}}'$

are the outer surface normals of the nanoparticle boundary at positions s, s', and we denote positions on and off the boundary with s and r, respectively. Similar expressions can be obtained for the magnetic field and the electromagnetic fields inside the nanoparticle. Equation (4) is reminiscent of Huygen's principle, which propagates the fields at the wavefront (here $\hat{n} \times E$, $\hat{n} \times H$) to another position in space (here r). Thus, once $\hat{n} \times E$, $\hat{n} \times H$ are known at the boundary, we can compute the electromagnetic fields everywhere else using the representation formula of Eq. (4).

We next do some extra work and rewrite Eq. (4) and the expressions for the remaining fields inside and outside the nanoparticle in a more compact form. First, we introduce the abbreviations $u_j^E(s) = \hat{n} \times E(s)$, $u_j^H(s) = \hat{n} \times H(s)$ for the tangential electromagnetic fields at the boundary inside ($j = 1$) and outside ($j = 2$). For the usual boundary conditions, the tangential electromagnetic fields are continuous when crossing the boundary, but for the modified boundary conditions of Eqs. (1), the fields are discontinuous and we thus keep the index j on $u_j^{E,H}$. We introduce the single and double layer potentials [6, Eqs. (5.34) and (5.35)],

$$[\mathbb{S}_j u](r) = \oint_{\partial\Omega} \overset{\leftrightarrow}{\boldsymbol{G}}_j(r, s') \cdot u(s') \, dS'$$
$$= \oint_{\partial\Omega} \left[g_j(r, s')u(s') + \frac{1}{k_j^2} \nabla g_j(r, s') \, \nabla' \cdot u(s') \right] dS' \tag{5a}$$

$$[\mathbb{D}_j u](r) = \oint_{\partial\Omega} \nabla' \times \overset{\leftrightarrow}{\boldsymbol{G}}_j(r, s') \cdot u(s') \, dS'$$
$$= \oint_{\partial\Omega} \nabla' \times g_j(r, s')u(s') \, dS', \tag{5b}$$

where $g_j(r, r')$ is the scalar Green's function given by the fraction on the right-hand side of Eq. (2). In obtaining the last expression in Eq. (5a), we have performed integration by parts and have used that the remaining contribution becomes zero for continuous tangential fields. If we assume that the nanoparticle is excited only through sources located within the background medium, we obtain for the representation formula inside the nanoparticle [6,34]

$$E(r) = -i\omega\mu_0 [\mathbb{S}_1 u_1^H](r) + [\mathbb{D}_1 u_1^E](r), \tag{6a}$$

$$H(r) = +i\omega\varepsilon_1 [\mathbb{S}_1 u_1^E](r) + [\mathbb{D}_1 u_1^H](r). \tag{6b}$$

Similarly, for positions r outside the particle, the electromagnetic fields can be obtained from

$$E(r) = E_2^{\text{inc}}(r) + i\omega\mu_0 [\mathbb{S}_2 u_2^H](r) - [\mathbb{D}_2 u_2^E](r), \tag{6c}$$

$$H(r) = H_2^{\text{inc}}(r) - i\omega\varepsilon_2 [\mathbb{S}_2 u_2^E](r) - [\mathbb{D}_2 u_2^H](r). \tag{6d}$$

The reader might like to check that Eqs. (4) and (6c) are indeed identical. The representation formulas of Eq. (6) can be used for two purposes. First, once the tangential electromagnetic fields are known at the boundary, we can compute the electromagnetic fields everywhere else. Second, they can be used to determine the tangential fields at the boundary themselves. To this end, we have to perform the limit $r \to s$ in Eq. (6), where the position r approaches the boundary from either the inside or outside, and exploit the boundary conditions

of the fields. While the limit can be performed safely for the single-layer potential, $\lim_{r \to s} \hat{n} \times [\mathbb{S}_j u](r) = \hat{n} \times [\mathbb{S}_j u](s)$, in the evaluation of the double layer potential we have to be careful on whether we approach the boundary from the inside or outside [6]:

$$\lim_{r \to s} \hat{n} \times [\mathbb{D}_{1,2} u](r) = \pm\frac{1}{2}u(s) + \hat{n} \times [\mathbb{D}_{1,2} u](s). \tag{7}$$

Here the positive sign has to be taken for the limit from the inside, and the negative sign for the limit from the outside. Thus, if we consider in Eqs. (6a) and (6b), the tangential fields $\hat{n} \times E$, $\hat{n} \times H$ and approach the boundary from the inside, we get

$$\frac{1}{2}u_1^E(s) = -i\omega\mu_0\hat{n} \times [\mathbb{S}_1 u_1^H](s) + \hat{n} \times [\mathbb{D}_1 u_1^E](s), \tag{8a}$$

$$\frac{1}{2}u_1^H(s) = +i\omega\varepsilon_1\hat{n} \times [\mathbb{S}_1 u_1^E](s) + \hat{n} \times [\mathbb{D}_1 u_1^H](s). \tag{8b}$$

Similarly, we obtain from Eqs. (6c) and (6d)

$$\frac{1}{2}u_2^E(s) = \hat{n} \times E_2^{\text{inc}}(s) + i\omega\mu_0\hat{n} \times [\mathbb{S}_2 u_2^H](s)$$
$$- \hat{n} \times [\mathbb{D}_2 u_2^E](s), \tag{8c}$$

$$\frac{1}{2}u_2^H(s) = \hat{n} \times H_2^{\text{inc}}(s) - i\omega\varepsilon_2\hat{n} \times [\mathbb{S}_2 u_2^E](s)$$
$$- \hat{n} \times [\mathbb{D}_2 u_2^H](s). \tag{8d}$$

Below we will show how to transform Eq. (8) into matrix equations using a BEM approach. Before doing so, we rewrite the boundary conditions of Eq. (1) using the tangential electromagnetic fields. The identity [35, Cor. 3.1.16]

$$\hat{n} \cdot \nabla \times u = -\nabla_\parallel \cdot (\hat{n} \times u)$$

and the curl equations $\nabla \times E = i\mu_0\omega H$, $\nabla \times H = -i\varepsilon\omega E$ enable us to express the normal components $E^\perp$, $H^\perp$ as

$$E_j^\perp = \hat{n} \cdot E_j = -\frac{i}{\varepsilon_j\omega}\nabla_\parallel \cdot u_j^H, \tag{9a}$$

$$H_j^\perp = \hat{n} \cdot H_j = \frac{i}{\mu_0\omega}\nabla_\parallel \cdot u_j^E. \tag{9b}$$

With this, the mesoscopic boundary conditions of Eqs. (1c) and (1d) for the tangential electromagnetic fields can be cast to the form

$$u_2^E - u_1^E = \frac{id_\perp}{\omega}\hat{n} \times \nabla_\parallel\nabla_\parallel \cdot \left(\frac{u_2^H}{\varepsilon_2} - \frac{u_1^H}{\varepsilon_1} \right), \tag{10a}$$

$$u_2^H - u_1^H = -i\omega d_\parallel \hat{n} \times (\varepsilon_2 u_2^E - \varepsilon_1 u_1^E). \tag{10b}$$

The remaining boundary conditions for the normal components are obtained by taking on both sides of Eqs. (10) the divergence $\nabla_\parallel \cdot$ along the boundary directions.

B. Boundary element method

We next submit the boundary integral Eq. (8) and the boundary conditions of Eq. (10) to a BEM and a Galerkin scheme. For that, let us introduce the pairing

$$\langle w, u \rangle = \oint_{\partial\Omega} w(s) \cdot u(s) \, dS, \tag{11}$$

where $w(s)$ is an arbitrary tangential vector function. We use this pairing to bring the boundary integral Eq. (8) and the boundary conditions Eq. (10) to a variational form which

is necessary to apply a Galerkin method. Equation (8a) is considered in the form

$$0 = \langle \hat{n} \times w, \tfrac{1}{2} u_1^E + i\omega\mu_0 \hat{n} \times \mathbb{S}_1 u_1^H - \hat{n} \times \mathbb{D}_1 u_1^E \rangle$$
$$= \langle w, -\tfrac{1}{2}\hat{n} \times u_1^E + i\omega\mu_0 \mathbb{S}_1 u_1^H - \mathbb{D}_1 u_1^E \rangle, \qquad (12a)$$

where we have used $\langle w, \hat{n} \times f \rangle = -\langle \hat{n} \times w, f \rangle$ and the identity $\hat{n} \times \hat{n} \times w = -w$. Similarly, we get for Eqs. (8b)–(8d)

$$\langle w, -\tfrac{1}{2}\hat{n} \times u_1^H - i\omega\varepsilon_1 \mathbb{S}_1 u_1^E - \mathbb{D}_1 u_1^H \rangle = 0, \qquad (12b)$$

$$\langle w, -\tfrac{1}{2}\hat{n} \times u_2^E - i\omega\mu_0 \mathbb{S}_2 u_2^H + \mathbb{D}_2 u_2^E \rangle = \langle w, E_2^{\text{inc}} \rangle \qquad (12c)$$

$$\langle w, -\tfrac{1}{2}\hat{n} \times u_2^H + i\omega\varepsilon_2 \mathbb{S}_2 u_2^E + \mathbb{D}_2 u_2^H \rangle = \langle w, H_2^{\text{inc}} \rangle. \qquad (12d)$$

Using the pairing of Eq. (11), we can employ integration by parts [35, Sec. 3.1] to shuffle around derivatives via

$$\oint_{\partial\Omega} w(s) \cdot \nabla_\parallel u(s)\, dS = -\oint_{\partial\Omega} (\nabla_\parallel \cdot w(s)) u(s)\, dS$$
$$= -\langle \nabla_\parallel \cdot w, u \rangle, \qquad (13)$$

where u is some scalar function, and in the last equality we have introduced a shorthand notation. This can be used to represent the single layer potential of Eq. (5a) on the boundary as

$$\langle w, \mathbb{S}_j u \rangle = \oint_{\partial\Omega} \left[w(s) \cdot u(s') - \frac{1}{k_j^2} (\nabla_\parallel \cdot w(s))(\nabla_\parallel \cdot u(s')) \right]$$
$$\times g_j(s, s')\, dS dS'. \qquad (14)$$

Submitting the boundary conditions of Eq. (10) to the pairing leads us to

$$\langle w, u_1^E \rangle - \frac{id_\perp}{\omega\varepsilon_1} \langle \nabla_\parallel \cdot \hat{n} \times w, \nabla_\parallel \cdot u_1^H \rangle$$
$$= \langle w, u_2^E \rangle - \frac{id_\perp}{\omega\varepsilon_2} \langle \nabla_\parallel \cdot \hat{n} \times w, \nabla_\parallel \cdot u_2^H \rangle$$
$$\langle w, u_1^H \rangle + i\omega\varepsilon_1 d_\parallel \langle w, \hat{n} \times u_1^E \rangle$$
$$= \langle w, u_2^H \rangle + i\omega\varepsilon_2 d_\parallel \langle w, \hat{n} \times u_2^E \rangle, \qquad (15)$$

where we have again employed Eq. (13) to simplify the $\nabla_\parallel \nabla_\parallel \cdot$ term, which would be hard to handle in a computational approach otherwise. In the BEM approach, we approximate the boundary through a discretization in terms of triangular boundary elements τ_i,

$$\partial\Omega \approx \bigcup_i \tau_i. \qquad (16)$$

For simplicity, we assume that all boundary elements τ_i have a triangular shape, although our approach would also work for other discretizations, e.g., using quadrilateral or mixed shapes. We additionally discretize the tangential fields u through Raviart-Thomas or Rao-Wilton-Glisson basis elements, see Fig. 1, which guarantee continuity of the tangential fields when going from one triangle to an adjacent one [6,34]. Technically, this is done by assigning to each edge ν of the discretized boundary a value for $[\![u]\!]_\nu$ and by using tangential basis functions f_ν^e that are nonzero in the two adjacent triangles only (a so-called local support), and which are constructed such that the outflow from one triangle equals the

inflow to the other triangle. For details, see Refs. [6,34]. The tangential fields can then be approximated through

$$\bar{u}_j^{E,H}(s) = \sum_{\nu=1}^n f_\nu^e(s) [\![u_j^{E,H}]\!]_\nu, \qquad (17)$$

where n is the total number of individual edges that determines the number of degrees of freedom for the BEM approach. Within the Galerkin scheme, we insert the functions $\bar{u}_j^{E,H}$ instead of $u_j^{E,H}$ in Eqs. (12) and (15) and use as test functions the basis functions f_ν^e. This gives

$$\langle f_\nu^e, -\tfrac{1}{2}\hat{n} \times \bar{u}_1^E + i\omega\mu_0 \mathbb{S}_1 \bar{u}_1^H - \mathbb{D}_1 \bar{u}_1^E \rangle = 0, \qquad (18a)$$

$$\langle f_\nu^e, -\tfrac{1}{2}\hat{n} \times \bar{u}_1^H - i\omega\varepsilon_1 \mathbb{S}_1 \bar{u}_1^E - \mathbb{D}_1 \bar{u}_1^H \rangle = 0, \qquad (18b)$$

$$\langle f_\nu^e, -\tfrac{1}{2}\hat{n} \times \bar{u}_2^E - i\omega\mu_0 \mathbb{S}_2 \bar{u}_2^h + \mathbb{D}_2 \bar{u}_2^E \rangle = \langle f_\nu^e, E_2^{\text{inc}} \rangle, \qquad (18c)$$

$$\langle f_\nu^e, -\tfrac{1}{2}\hat{n} \times \bar{u}_2^H + i\omega\varepsilon_2 \mathbb{S}_2 \bar{u}_2^E + \mathbb{D}_2 \bar{u}_2^H \rangle = \langle f_\nu^e, H_2^{\text{inc}} \rangle, \qquad (18d)$$

and

$$\langle f_\nu^e, \bar{u}_1^E \rangle - \frac{id_\perp}{\omega\varepsilon_1} \langle \nabla_\parallel \cdot \hat{n} \times f_\nu^e, \nabla_\parallel \cdot \bar{u}_1^H \rangle$$
$$= \langle f_\nu^e, \bar{u}_2^E \rangle - \frac{id_\perp}{\omega\varepsilon_2} \langle \nabla_\parallel \cdot \hat{n} \times f_\nu^e, \nabla_\parallel \cdot \bar{u}_2^H \rangle$$
$$\langle f_\nu^e, \bar{u}_1^H \rangle + i\omega\varepsilon_1 d_\parallel \langle f_\nu^e, \hat{n} \times \bar{u}_1^E \rangle$$
$$= \langle f_\nu^e, \bar{u}_2^H \rangle + i\omega\varepsilon_2 d_\parallel \langle f_\nu^e, \hat{n} \times \bar{u}_2^E \rangle. \qquad (19)$$

These equations are used to determine the unknown expansion coefficients $[\![u^{E,H}]\!]_\nu$. Combining the electric and magnetic components of the solution vectors according to

$$u_j = \begin{pmatrix} [\![u_j^E]\!] \\ [\![u_j^H]\!] \end{pmatrix}, \qquad (20)$$

we rewrite Eq. (18) in the compact form

$$\left(\tfrac{1}{2}I - A_1 \right) u_1 = 0, \qquad (21a)$$

$$\left(\tfrac{1}{2}I + A_2 \right) u_2 = q. \qquad (21b)$$

A more detailed discussion, as well as a definition of the matrices I and A_j is given in Appendix. Equation (21) is usually referred to as the Calderon identities. To solve for the unknowns u_1, u_2, we have to combine the two equations and invoke the boundary conditions of Eq. (19), which can be cast to the form

$$B_1 u_1 = B_2 u_2, \qquad (22)$$

with the matrices B_1, B_2 given in Eq. (A8). This expression together with the Calderon identities of Eq. (21) allow us to obtain the desired solutions. We here introduce a scheme that is inspired by the Poggio-Miller-Chang-Harrington-Wu-Tsai formulation [36–38] where the two Calderon identities are subtracted:

$$\left[\left(\tfrac{1}{2}I + A_2 \right) - \left(\tfrac{1}{2}I - A_1 \right) B_1^{-1} B_2 \right] u_2 = q. \qquad (23)$$

The $B_1^{-1} B_2$ term accounts for the modified boundary conditions, which would become one for the case where both Feibelman parameters are set to zero. Thus, the solution of the BEM equations, namely, the inversion of the term in brackets of Eq. (23), is highly similar to the usual solution
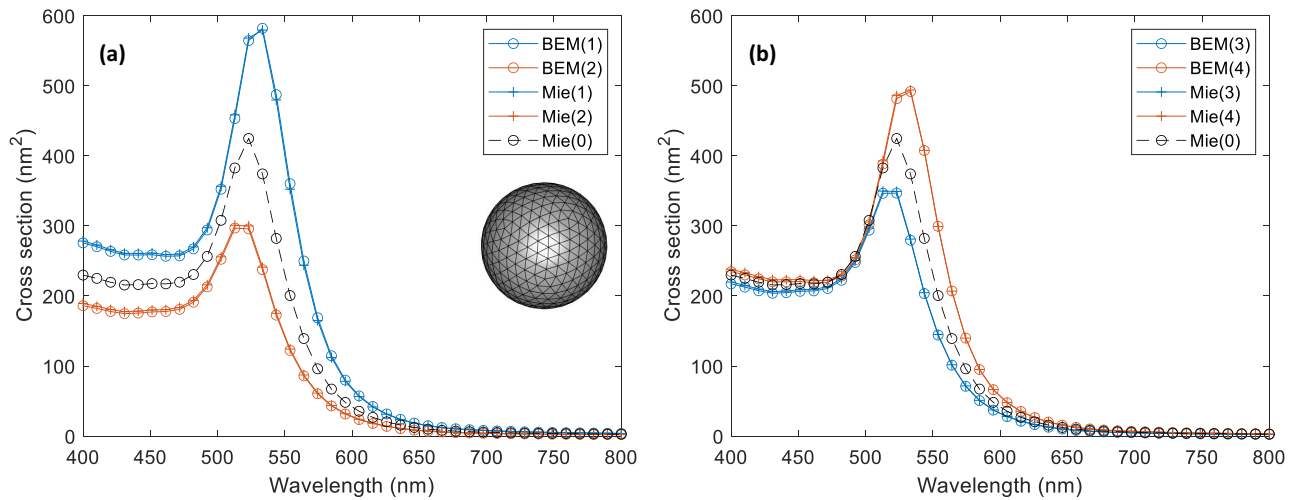
FIG. 2. Extinction cross sections for gold nanosphere (diameter 20 nm, dielectric function taken from Ref. [39]) embedded in water (refractive index $n_b = 1.33$). We use large and frequency-independent Feibelman parameters of (1) $d_\perp = 0.5$ nm, $d_\parallel = 0$, (2) $d_\perp = -0.5$ nm, $d_\parallel = 0$, (3) $d_\perp = 0$, $d_\parallel = 0.5$ nm, (4) $d_\perp = 0$, $d_\parallel = -0.5$ nm. The circle symbols report results of our BEM approach using the sphere discretization with 400 vertices shown in the inset of (a), the cross symbols report results of Mie theory including Feibelman parameters. BEM and Mie results are in perfect agreement throughout. The dashed line shows for comparison results of standard Mie theory without Feibelman parameters.

scheme. Once the tangential electromagnetic fields u_2 are known, we can compute the fields everywhere in the embedding medium using the representation formulas of Eq. (6). The solution u_1 inside the nanoparticle can be obtained through $u_1 = B_1^{-1} B_2 u_2$.

III. RESULTS

We have implemented the working Eq. (23) in our homemade BEM solver NANOBEM [40]. Figure 2 shows results for an optically excited gold nanosphere with 20 nm diameter, which is embedded in water. For the permittivity function we use tabulated values extracted from an optical experiment [39]. We set the Feibelman parameters $d_\perp$, $d_\parallel$ to constant but otherwise arbitrary values, which are reported in the figure caption, and compare our results with those of a Mie theory including Feibelman parameter [24]. As can be seen in the figure, the results of our BEM simulations and Mie theory are in perfect agreement and almost indistinguishable throughout, thus demonstrating the accuracy of our computational approach. We will comment on the performance of our modified BEM approach further below in Sec. IV. Quite generally, with this proof-of-principle result, we are now in the position to perform simulations including Feibelman parameters for any other setup that can be modeled within a BEM approach. In the following, we discuss two simple setups, namely, coupling of nanoparticles and the computation of resonance modes, mainly to demonstrate the potential of our scheme. More detailed investigations, including also Feibelman parameters extracted from *ab initio* calculations, will be presented elsewhere.

In the following, we use a Drude dielectric function representative for gold [18], with a plasma frequency of $\hbar\omega_p = 3.3$ eV and a damping constant $\hbar\gamma = 0.165$ eV, together with

the Feibelman parameters for the hydrodynamic model [23]:

$$d_\perp(\omega) = -\frac{\beta}{\sqrt{\omega_p^2 - \omega^2}}, \quad d_\parallel = 0. \quad (24)$$

The β parameter accounts for the hydrodynamic pressure of an electron gas, its value of $\beta = 0.0063\,c$ is taken from Ref. [18]. Figure 3 shows the optical spectra for two coupled gold nanospheres and for different gap distances. One
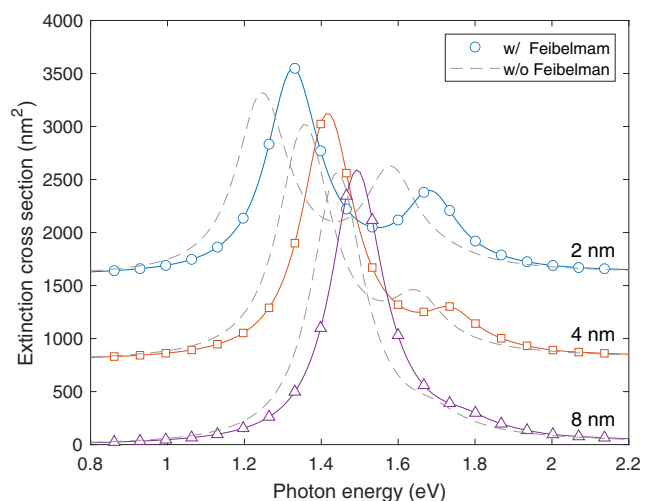

FIG. 3. Extinction cross section for coupled gold nanospheres with a diameter of 20 nm and for gap distances of 2, 4, and 8 nm, as indicated on the right-hand side (we use $n_b = 1.33$). The spectra are offset for clarity, and the polarization of the incoming light is along the symmetry axis of the coupled spheres. The two peaks are associated with bonding and anti-bonding dimer modes, and the splitting increases with decreasing gap distance owing to the increased coupling strength.
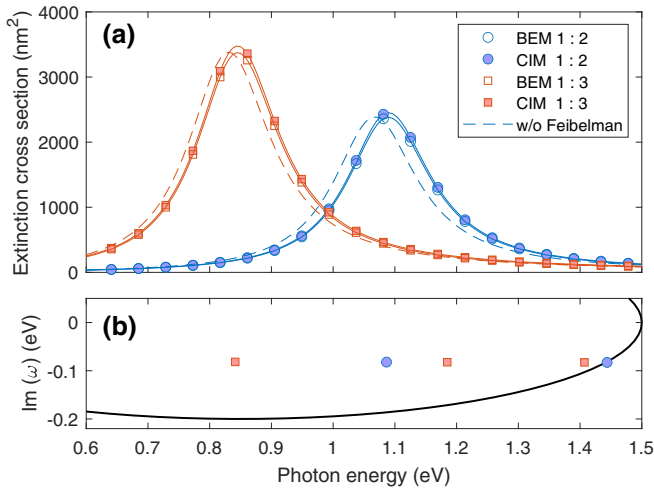
FIG. 4. Computation of resonance modes and optical spectra for nanoellipsoids using a dielectric function representative for gold [18]. (a) Extinction cross sections for prolate nanoellipsoids with a short axis of 20 nm and a long axis of 40 nm (circles) and 60 nm (squares); the polarization of the incoming light is parallel to the long axis. The open symbols show results from the full BEM simulations, the open symbols from the resonance mode approximation, and the dashed lines from simulations without Feibelman parameters. (b) Complex frequency plane. The solid line shows the contour used in the computation of the resonance modes and the symbols the location of the resonance mode energies.

observes two peaks associated with the bonding and antibonding dimer modes [6], and the peak splitting increases with decreasing gap distance owing to the enhanced coupling between the spheres. For the chosen parameters, the simulation results with (solid lines) and without (dashed lines) consideration of Feibelman parameters are similar, apart from an approximately constant shift.

As a final example, in Fig. 4 we show results of simulations with resonance or quasinormal modes [28–32] for gold nanoellipsoids, following the prescription given in Refs. [40,41]. Importantly, the calculation of the resonance modes is almost identical for simulations with and without mesoscopic boundary conditions, with the exception of the additional boundary matrices to be considered in Eq. (23) [42]. Figure 4(b) shows the complex resonance energies obtained from our contour integral method [40,41], and Fig. 4(a) the extinction spectra obtained from the full BEM simulations (open symbols) and the resonance mode expansions (full symbols). We observe that the spectra are in perfect agreement. The simulation results presented in Figs. 3 and 4 demonstrate that all simulations that can be performed with standard BEM solvers can indeed be equally well performed with BEM solvers incorporating mesosocopic boundary conditions.

IV. DISCUSSION AND SUMMARY

We finally comment on the computer times for BEM simulations with and without mesoscopic boundary conditions, which is related to the additional computation of the $B_1^{-1}B_2$ term in Eq. (23). For coarse boundary discretizations with a few hundred boundary elements, the main computational cost
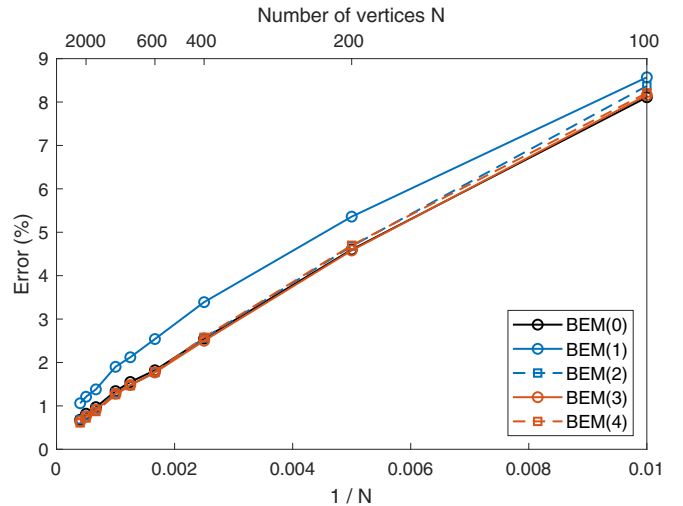

FIG. 5. Error between tangential electric fields computed within Mie theory and BEM simulations, evaluated at the centroids of the boundary elements, see Eq. (25). We consider a gold nanosphere with 20 nm diameter and the same material and simulation parameters as listed in the caption of Fig. 2, and compare simulation results for boundary discretizations with a varying number of vertices N and for a wavelength of 520 nm. With decreasing mesh size, the error becomes smaller monotonously.

is the evaluation of the single and double layer potentials, see Eq. (A1), and the evaluation and inversion of the boundary matrices B_1, B_2 leads to no significant overhead. Things may change for finer discretizations with a few thousand boundary elements, where simulations can be slowed down by a factor between 2 and 3 in comparison to normal BEM simulations. For nanoparticles with separated boundaries, such as for coupled or coated particles, the evaluation of $B_1^{-1}B_2$ can be done blockwise, which leads to a significant speedup and comparable computer times for simulations with and without mesoscopic boundary conditions. Thus, the additional overhead in Eq. (23) is usually small.

In Fig. 5, we investigate the accuracy of our BEM implementation. We consider a gold nanosphere with 20-nm diameter and use the same material and simulation parameters as listed in the caption of Fig. 2, and compare simulation results for boundary discretizations with a varying number of vertices N and correspondingly boundary elements. For each discretization, we compute the tangential electric fields at the centroids of the boundary elements and evaluate the deviations from the exact fields obtained within Mie theory:

$$\text{error} = \sqrt{\frac{\sum_i \left| \hat{\boldsymbol{n}}_i \times \left(\boldsymbol{E}_i^{\text{BEM}} - \boldsymbol{E}_i^{\text{Mie}} \right) \right|^2}{\sum_i^n \left| \hat{\boldsymbol{n}}_i \times \boldsymbol{E}_i^{\text{Mie}} \right|^2}}. \quad (25)$$

As can be seen in Fig. 5, the error decreases monotonously when increasing the number of vertices, where all simulation setups exhibit a similar error slope. This demonstrates the accuracy and robustness of the scheme described in this paper.

To summarize, we have presented a methodology for the implementation of mesoscopic boundary conditions within a BEM approach, and have demonstrated that the results of such

an approach are in perfect agreement with Mie theory. Further case studies have revealed that our implementation can be used in all situations where normal BEM simulations can be employed, and that the computational overhead is negligible to moderate in most cases of interest. This establishes BEM as a viable and efficient solution scheme for nanoscale electromagnetism, including mesoscopic boundary conditions.

ACKNOWLEDGMENTS

APPENDIX

In this Appendix, we provide further details for the derivation of Eqs. (21) and (22). With the shape functions of Eq. (17), we introduce the matrix elements for the discretized single- and double-layer potentials

$$
[\![\mathbb{S}]\!]_{\nu\nu'} = \oint \oint \left[\boldsymbol{f}_\nu^e(\boldsymbol{s}) \cdot \boldsymbol{f}_{\nu'}^e(\boldsymbol{s}') - \frac{\boldsymbol{\nabla}_\| \cdot \boldsymbol{f}_\nu^e(\boldsymbol{s})\, \boldsymbol{\nabla}_\|' \cdot \boldsymbol{f}_{\nu'}^e(\boldsymbol{s}')}{k^2} \right] \\
\times g(\boldsymbol{s}, \boldsymbol{s}')\, dS\, dS', \tag{A1a}
$$

$$
[\![\mathbb{D}]\!]_{\nu\nu'} = \oint \oint \boldsymbol{f}_\nu^e(\boldsymbol{s}) \cdot \boldsymbol{\nabla}' g(\boldsymbol{s}, \boldsymbol{s}') \times \boldsymbol{f}_{\nu'}^e(\boldsymbol{s}')\, dS\, dS', \tag{A1b}
$$

together with the matrix

$$
[\![I]\!]_{\nu\nu'} = \langle \boldsymbol{f}_\nu^e, \hat{\boldsymbol{n}} \times \boldsymbol{f}_{\nu'}^e \rangle. \tag{A2}
$$

For the incoming fields, we introduce the inhomogeneities

$$
[\![q^E]\!]_\nu = \langle \boldsymbol{f}_\nu^e, \boldsymbol{E}_2^{\text{inc}} \rangle, \tag{A3a}
$$

$$
[\![q^H]\!]_\nu = \langle \boldsymbol{f}_\nu^e, \boldsymbol{H}_2^{\text{inc}} \rangle, \tag{A3b}
$$

and combine the electric and magnetic components in a single vector $q = ([\![q_E]\!], [\![q_H]\!])^T$, in complete analogy to Eq. (20). Together with the block matrices

$$
I = -\begin{pmatrix} [\![I]\!] & 0 \\ 0 & [\![I]\!] \end{pmatrix}, \quad A_j = \begin{pmatrix} [\![\mathbb{D}_j]\!] & -i\mu_0\omega[\![\mathbb{S}_j]\!] \\ i\varepsilon_j\omega[\![\mathbb{S}_j]\!] & [\![\mathbb{D}_j]\!] \end{pmatrix}, \tag{A4}
$$

we are then led to our final Eq. (21). For evaluating the boundary conditions within the Galerkin scheme, we introduce the matrices

$$
[\![J]\!]_{\nu\nu'} = \langle \boldsymbol{f}_\nu^e, \boldsymbol{f}_{\nu'}^e \rangle, \tag{A5}
$$

$$
[\![K]\!]_{\nu\nu'} = \langle \boldsymbol{\nabla}_\| \cdot \boldsymbol{f}_\nu^e, \boldsymbol{\nabla}_\| \cdot \boldsymbol{f}_{\nu'}^e \rangle. \tag{A6}
$$

Inspection of Eq. (15) shows that we have to deal with a term of the form $\langle \boldsymbol{\nabla}_\| \cdot \hat{\boldsymbol{n}} \times \boldsymbol{f}_\nu^e, \boldsymbol{\nabla}_\| \cdot \boldsymbol{f}_{\nu'}^e \rangle$ rather than with the expression of Eq. (A6). Any pairing between two functions $\boldsymbol{u}$, $\boldsymbol{v}$ can be rewritten by inserting the identity operator expanded in the nonorthogonal basis of the shape elements via

$$
\langle \boldsymbol{u}, \boldsymbol{v} \rangle = \sum_{\nu\nu'} \langle \boldsymbol{u}, \boldsymbol{f}_\nu^e \rangle ([\![J]\!]^{-1})_{\nu\nu'} \langle \boldsymbol{f}_{\nu'}^e, \boldsymbol{v} \rangle. \tag{A7}
$$

With this, we then find $\langle \boldsymbol{\nabla}_\| \cdot \hat{\boldsymbol{n}} \times \boldsymbol{f}_\nu^e, \boldsymbol{\nabla}_\| \cdot \boldsymbol{f}_{\nu'}^e \rangle = -([\![I]\!][\![J]\!]^{-1}[\![K]\!])_{\nu\nu'}$, where the negative sign is because of the reversed order of pairing functions in $\langle \hat{\boldsymbol{n}} \times \boldsymbol{f}_\nu^e, \boldsymbol{f}_{\nu'}^e \rangle$ in comparison to the matrix of Eq. (A2). We are thus finally led to Eq. (22) with the matrix

$$
B_j = \begin{pmatrix} [\![J]\!] & -\frac{i}{\omega\varepsilon_j} d_\perp [\![\tilde{K}]\!] \\ i\omega\varepsilon_j d_\| [\![I]\!] & [\![J]\!] \end{pmatrix}, \tag{A8}
$$

where we have introduced $[\![\tilde{K}]\!] = -[\![I]\!][\![J]\!]^{-1}[\![K]\!]$.

[1] W. L. Barnes, A. Dereux, and T. W. Ebbesen, Nature (London) **424**, 824 (2003).

[2] H. Atwater, Sci. Am. **296**, 56 (2007).

[3] J. A. Schuller, E. S. Barnard, W. Cai, Y. C. Jun, J. S. White, and M. L. Brongersma, Nature Mat. **9**, 193 (2010).

[4] L. Novotny and N. van Hulst, Nat. Photonics **5**, 83 (2011).

[5] S. A. Maier, *Plasmonics: Fundamentals and Applications* (Springer, Berlin, 2007).

[6] U. Hohenester, *Nano and Quantum Optics* (Springer, Cham, Switzerland, 2020).

[7] J. D. Caldwell, L. Lindsay, V. Giannini, I. Vurgaftman, T. L. Reinecke, S. A. Maier, and O. J. Glembocki, Nanophotonics **4**, 44 (2015).

[8] M. Maldovan, Nature (London) **503**, 209 (2013).

[9] G. S. Snyder and E. S. Toberer, Nat. Meter. **7**, 105 (2008).

[10] K. Joulain, J.-P. Mulet, F. Marquier, R. Carminati, and J.-J. Greffet, Surf. Sci. Rep. **57**, 59 (2005).

[11] A. I. Volokitin and B. N. J. Persson, Rev. Mod. Phys. **79**, 1291 (2007).

[12] U. Kreibig and M. Vollmer, *Optical Properties of Metal Clusters*, Springer Series in Material Science Vol. 25 (Springer, Berlin, 1995).

[13] M. S. Tame, K. R. McEnery, S. K. Ozdemir, J. Lee, S. A. Maier, and M. S. Kim, Nat. Phys. **9**, 329 (2013).

[14] *Quantum Plasmonics*, edited by S. I. Bozhevolnyi, L. Martin-Moreno, and F. Garcia-Vidal (Springer, Cham, Switzerland, 2017).

[15] N. A. Mortensen, Nanophotonics **10**, 2563 (2021).

[16] C. David and F. J. García de Abajo, J. Phys. Chem. C **115**, 19470 (2011).

[17] C. Ciraci, R. T. Hill, Y. Urzhumov, A. I. Fernandez-Dominguez, S. A. Maier, J. B. Pendry, A. Chilkoti, and D. R. Smith, Science **337**, 1072 (2012).

[18] Y. Luo, A. I. Fernandez-Dominguez, A. Wiener, S. A. Maier, and J. B. Pendry, Phys. Rev. Lett. **111**, 093901 (2013).

[19] N. A. Mortensen, S. Raza, M. Wubs, T. Sondergaard, and S. I. Bozhevolnyi, Nat. Commun. **5**, 3809 (2014).

[20] R. Esteban, A. G. Borisov, P. Nordlander, and J. Aizpurua, Nat. Commun. **3**, 825 (2012).

[21] R. Esteban, A. Zugarramurdi, P. Zhang, P. Nordlander, F. J. Garcia-Vidal, A. G. Borisov, and J. Aizpurua, Faraday Discuss. **178**, 151 (2015).

[22] K. J. Savage, M. M. Hawkeye, R. Esteband, A. G. Borisov, J. Aizpurua, and J. J. Baumberg, Nature (London) **491**, 574 (2012).

[23] P. J. Feibelman, Prog. Surf. Sci. **12**, 287 (1982).

[24] P. A. D. Goncalves, T. Christensen, N. Rivera, A.-P. Jauho, N. A. Mortensen, and M. Soljcic, Nat. Commun. **11**, 366 (2020).

[25] T. V. Teperik, P. Nordlander, J. Aizpurua, and A. G. Borisov, Phys. Rev. Lett. **110**, 263901 (2013).

[26] Y. Yang, D. Zhu, W. Yan, A. Agarwal, M. Zheng, J. D. Joannopoulos, P. Lalanne, T. Christensen, K. K. Berggren, and M. Soljacic, Nature (London) **576**, 248 (2019).

[27] J. D. Jackson, *Classical Electrodynamics* (Wiley, New York, 1999).

[28] P. T. Leung, S. Y. Liu, and K. Young, Phys. Rev. A **49**, 3057 (1994).

[29] P. T. Kristensen, C. Van Vlack, and S. Hughes, Opt. Lett. **37**, 1649 (2012).

[30] C. Sauvan, J. P. Hugonin, I. S. Maksymov, and P. Lalanne, Phys. Rev. Lett. **110**, 237401 (2013).

[31] P. Lalanne, W. Yan, A. Gras, C. Sauvan, J.-P. Hugonin, M. Besbes, G. Demesy, M. D. Truong, B. Gralak, F. Zolla *et al.*, J. Opt. Soc. Am. A **36**, 686 (2019).

[32] P. T. Kristensen, K. Herrmann, F. Intravaia, and K. Busch, Adv. Opt. Photon. **12**, 612 (2020).

[33] J. A. Stratton and L. J. Chu, Phys. Rev. **56**, 99 (1939).

[34] W. C. Chew, *Waves and Fields in Inhomogeneous Media* (IEEE Press, Picsatoway, 1995).

[35] F. Assous, P. Ciarlet, and S. Labrunie, *Mathematical Foundations of Computational Electromagnetism* Vol. 198 of *Applied Mathematical Sciences* (Springer, Cham, Switerzland, 2018).

[36] Y. Chang and R. Harrington, IEEE Trans. Antennas Propag. **25**, 789 (1977).

[37] A. J. Poggio and E. K. Miller, in *Computer Techniques for Electromagnetics*, International Series of Monographs in Electrical Engineering, edited by R. Mittra (Pergamon, Oxford, 1973), pp. 159–264.

[38] T. K. Wu and L. L. Tsai, Radio Sci. **12**, 709 (1977).

[39] P. B. Johnson and R. W. Christy, Phys. Rev. B **6**, 4370 (1972).

[40] U. Hohenester, N. Reichelt, and G. Unger (unpublished).

[41] G. Unger, A. Trügler, and U. Hohenester, Phys. Rev. Lett. **121**, 246802 (2018).

[42] In comparison to the contour integral method discussed in Ref. [40], we have to compute the left eigenvectors numerically because the transmission matrix of Eq. (23) is no longer symmetric.